

Electric polarization driven by non-collinear spin alignment investigated by first principles calculations

Sergiy Mankovsky*,¹ Svitlana Polesya,¹ Jan Minar,² and Hubert Ebert¹

¹Department of Chemistry/Phys. Chemistry, LMU Munich,
Butenandtstrasse 11, D-81377 Munich, Germany*

²New Technologies Research Center, University of West Bohemia, 30100 Pilsen, Czech Republic

(Dated: December 2, 2025)

We present an approach for first principles investigations on the spin driven electric polarization in type II multiferroics. We propose a parametrization of the polarization with the parameters calculated using the Korringa-Kohn-Rostoker Green function (KKR-GF) formalism. Within this approach the induced electric polarization of a unit cell is represented in terms of three-site parameters. Those antisymmetric with respect to spin permutation are seen as an ab-initio based counter-part to the phenomenological parameters used within the inverse-Dzyaloshinskii-Moriya-interaction (DMI) model. Due to their relativistic origin, these parameters are responsible for the electric polarization induced in the presence of a non-collinear spin alignment in materials with a centrosymmetric crystal structure. Beyond to this, our approach gives direct access to the element- or site-resolved electric polarization. To demonstrate the capability of the approach, we consider several examples of the so-called type II multiferroics, for which the magneto-electric effect is observed either as a consequence of an applied magnetic field (we use Cr_2O_3 as a prototype), or as a result of a phase transition to a spin-spiral magnetic state, as for instance in MnI_2 , CuCrO_2 and AgCrO_2 .

I. INTRODUCTION

The growing interest in multiferroic materials is motivated by the possibility to control their magnetic or electric polarization by applying external electric or magnetic fields, respectively [1–4], allowing various technical applications in electronics, spintronics, etc. [5]. In particular, applying a static magnetic or electric field to control the properties of multiferroic materials, one can minimize the energy losses caused by induced electric currents. This feature is a consequence of coexisting ferroelectricity (FE) and ferromagnetism (FM) in multiferroic systems, which obey individually different symmetry requirements, either broken space inversion symmetry \mathcal{I} or broken time reversal symmetry \mathcal{T} , respectively, however, with the combined \mathcal{IT} symmetry being conserved.

While there are different types of multiferroics discussed in the literature (see, e.g. [2, 3, 6–8]), we will focus here on the materials which belong to the so-called type-II multiferroics, in which electric polarization appears only in the magnetically ordered phase due to a strong coupling between magnetism and ferroelectricity. Any perturbation in these materials, breaking time reversal symmetry \mathcal{T} , gives rise to an electric polarization being allowed as a result of broken inversion symmetry \mathcal{I} [2, 9–11]. This occurs in collinear antiferromagnetic (AFM) systems, where an electrical polarization can appear as a consequence of an applied magnetic field, as it was observed, for instance, in β Cr_2O_3 [12–14]. In this case, the linear magneto-electric (ME) effect is described by the ME tensor $\underline{\alpha}$ giving the induced electric

polarization \vec{P} via the relationship $\vec{P} = \underline{\alpha} \vec{H}$. As an example for the spontaneous ME effect, one can mention the triangular-lattice AFM compounds (TLA) such as MnI_2 , CuFeO_2 , CuCrO_2 , AgCrO_2 , etc. These materials undergo a phase transition at low temperature to a non-collinear magnetic state [15–19], as a consequence of the competition of the frustrated AFM exchange interactions. In this work, however, we do not discuss the magnetic properties of these materials nor the mechanisms responsible for the stabilization of the AFM state, focusing instead on the electric polarization for different non-collinear magnetic structures.

Despite common symmetry requirements, the microscopic mechanism for the ME effect in the type II multiferroics may differ for different materials [10, 20]. The spin-orbit driven mechanism suggested by Katsura, Nagaosa and Balatsky (KNB) was interpreted in terms of the spin current [21] appearing between the two spin moments due to their non-collinear alignment. Using the simplified model of two interacting transition metal atoms with non-collinear spin moments \hat{s}_1 and \hat{s}_2 on sites 1 and 2, respectively, they have shown that the induced electric polarization follows the expression $\vec{P}_{12} \sim \vec{e}_{12} \times (\hat{s}_1 \times \hat{s}_2)$ with $\vec{e}_{12} = \vec{R}_{12}/|\vec{R}_{12}|$, where \vec{R}_{12} is the vector connecting the two sites. This mechanism explains well the ferroelectricity in multiferroics with a cycloidal spin-spiral order [22–24]. A similar result can be obtained applying the phenomenological theory of inhomogeneous ferroelectric magnets to systems with cubic symmetry, as was shown by Mostovoy [9]. The expression given above [21] is often used to explain the origin of the spin-induced electric polarization. On the other hand, the KNB theory may fail to explain the experimental results on the electric polarization in materials with a proper screw type magnetic order (for example CuFeO_2 [25, 26] and MnI_2

* Sergiy.Mankovsky@cup.uni-muenchen.de

[27]), as was pointed out by Solovyev [28] and other authors. For that reason, other mechanisms were suggested to explain the observed magneto-electric effect in these materials. For instance, the electric polarization in CuFeO₂ having a helimagnetic structure was attributed to the single-ion effect due to the spin-dependent $p - d$ hybridization [7, 26]. A mechanism alternative to that of KNB was suggested by Sergienko and Dagotto [29], which postulates an electric polarization appearing due to the spin-orbit-coupling (SOC) driven atomic displacements induced by the non-collinear spin alignment. This mechanism is discussed in terms of the Dzyaloshinskii-Moriya interaction, which may be responsible for the stabilization of helical magnetic order in the presence of atomic displacements that break the inversion symmetry in the system. Accordingly, it is referred to in the literature as the inverse-DMI mechanism.

To go beyond the phenomenological model treatment of the ME effect, a more general approach based on the density functional theory (DFT) calculations has been used [23, 28, 30]. While direct DFT-based calculations, require supercell calculations, which may be time-consuming in the case of long-period spin spiral structures, the electric polarization can be parametrized for the sake of simplicity, and represented in terms of two-site polarization parameters. A simplification can be achieved by the parametrization scheme given for instance by Xiang et al. [30] within their generalized KNB model, or suggested by Solovyev [28] using the Berry-phase theory for the effective half-filled Hubbard model. The latter approach was successfully applied to describe the spin-induced electric polarization in different multi-ferroic materials [28, 31, 32]. Furthermore, this theory allowed the authors to analyze the origin of the restrictions of the KNB theory [11]. Recently, the approach based on the generalized KNB model [30] was used also for first principles investigations of the ME effect for topological solitons in 2D CrI₃ monolayers. Note that the mechanisms mentioned above are seen as a 'pure electronic' contribution to the induced polarization. This means that for some materials an essential contribution to the ME effect may be associated with the inverse-DMI mechanism [29] due to ion displacements from their centrosymmetric positions, as it was shown for instance for RMnO₃, ($R = \text{Gd, Tb, Dy}$) [23, 29].

We will focus in the following on the 'pure electronic' effect, using the approach described in the Section II, representing the parametrization of the electric polarization in full analogy to the parametrization of the spin-lattice Hamiltonian [33, 34]. The corresponding parameters are calculated from first principles via the Green function (GF) technique implemented using the Korringa-Kohn-Rostoker (KKR), or multiple scattering theory (MST) band structure method leading to the KKR-GF scheme. In the following sections we apply this approach to different materials demonstrating the properties which can be discussed on the basis of such calculations.

II. THEORETICAL DETAILS

In a recent study [33, 34] we discussed the spin-lattice interaction represented by the coupling tensors $J_{ij,k}$ which allows to get the force on an atom at \vec{R}_k generated due to the perturbation caused by the rotation of the spin moments \hat{s}_i and \hat{s}_j on sites i and j , respectively. Using the same idea for the magnetically induced electric polarization $\Delta\vec{P}$, we start with the definition

$$\Delta\vec{P} = \frac{1}{\Omega} \int d^3r e\vec{r} \Delta\rho(\vec{r}) . \quad (1)$$

In the case of a solid with $N_{u.c.}$ atoms per unit cell which are specified by the basis vectors t_q ($q = 1, N_{u.c.}$) and have an associated volume Ω_q , the integral in Eq. (1) can be written as follows

$$\begin{aligned} \Delta\vec{P} &= \frac{e}{\Omega} \sum_n \sum_q \int_{\Omega_q} d^3r [\vec{r}_q + \vec{R}_n + \vec{t}_q] \Delta\rho(\vec{r}_q) \\ &= \frac{e}{\Omega} \left[\sum_n \sum_q \int_{\Omega_q} d^3r_q \vec{r}_q \Delta\rho(\vec{r}_q) \right. \\ &\quad + \sum_n \vec{R}_n \sum_q \int_{\Omega_q} d^3r_q \Delta\rho(\vec{r}_q) \\ &\quad \left. + \sum_n \sum_q \vec{t}_q \int_{\Omega_q} d^3r_q \Delta\rho(\vec{r}_q) \right] . \end{aligned} \quad (2)$$

Here \vec{R}_n is a Bravais vector that describes the position of the unit cell, and $\vec{r}_q = \vec{r} - \vec{R}_n - \vec{t}_q$ are atom cell centered coordinates. The second term in Eq. (2) vanishes due to charge neutrality of the unit cell. The third term describes the change of the dipole moment of the unit cell due to a charge redistribution within the cell. This term is not discussed here, as we focus on the polarization due to a charge distortion under the assumption of charge conservation for each atom. Therefore, we can simplify the expression above to the form

$$\Delta\vec{P} \approx \sum_q \frac{1}{\Omega_{u.c.}} \int_{\Omega_q} d^3r_q \vec{r}_q \Delta\rho(\vec{r}_q) = \sum_q \Delta\vec{P}_q , \quad (3)$$

giving the induced electric polarization of a unit cell after summation over the induced dipole moments of all atoms in the cell. This is seen as an on-site approximation assuming a pronounced localization of the electronic states contributing to the electric polarization of the atoms. As a consequence, for each site q we will discuss the dipole moment evaluated with respect to the site origin, which is induced by all contributions associated with spin rotations of the surrounding atoms i and j .

In general, Eq. (3) obviously may represent the change of the local polarization on lattice site q as a response to a perturbation induced by a rotation of magnetic moments. Here we restrict ourselves to systems with a centrosymmetric crystal lattice and invariant with respect to time

reversal in its reference state. This implies that a finite electric polarization may occur only as a consequence of spin rotations creating a non-collinear magnetic structure.

In terms of the electronic Green function the electric polarization can be written as follows

$$\Delta \vec{P} = -\frac{1}{\pi} \text{Im} \text{Tr} \int dE \frac{1}{\Omega_{\text{u.c.}}} \times \sum_q \int_{\Omega_q} d^3 r_q (e \vec{r}_q) \Delta G(\vec{r}_q, \vec{r}_q, E). \quad (4)$$

In the presence of a perturbation $\Delta V(\vec{r})$, the corresponding change of the Green function occurring in Eq. 4 is given up to second order by

$$\Delta G(E) = G_0(E) \Delta V G_0(E) + G_0(E) \Delta V G_0(E) \Delta V G_0(E) + \dots, \quad (5)$$

with $G_0(E)$ the Green function of the system in its unperturbed reference state. For the sake of simplicity, we omit the arguments \vec{r} for the potential and Green functions, keeping in mind an integration over the region of the applied perturbation. In the case of perturbations due to spin tiltings on two lattice sites i and j one can ignore the first order term in Eq. 5 and obtains

$$\Delta \vec{P} = -\frac{1}{\pi} \frac{e}{\Omega_{\text{u.c.}}} \text{Im} \text{Tr} \int dE \sum_q \int_{\Omega_q} d^3 r_q \int d^3 r' \int d^3 r'' \vec{r} G(\vec{r}_q, \vec{r}', E) \Delta V_i(\vec{r}') \times G(\vec{r}', \vec{r}'', E) \Delta V_j(\vec{r}'') G(\vec{r}'', \vec{r}_q, E). \quad (6)$$

With this, one can introduce the parameters $\mathcal{P}_{ij,k}^{\alpha\beta,\mu}$ defined as derivatives with respect to the spin direction on sites i ($\vec{R}_i = \vec{R}_{n_i} + \vec{t}_{q_i}$) and j ($\vec{R}_j = \vec{R}_{n_j} + \vec{t}_{q_j}$), Δs_i^α and Δs_j^β , respectively, giving the polarization on site k with $\vec{R}_k = \vec{t}_{q_k}$ in the unit cell $\vec{R}_{n_k} = 0$, as follows

$$\Delta P^\mu = \sum_{i,j,k} \frac{\partial^2 (\Delta P_k^\mu)(\{\hat{s}_n\})}{\partial s_i^\alpha \partial s_j^\beta} \Delta s_i^\alpha \Delta s_j^\alpha = \sum_{i,j,k} \mathcal{P}_{ij,k}^{\alpha\beta,\mu} \Delta s_i^\alpha \Delta s_j^\alpha. \quad (7)$$

Later on we will distinguish symmetric and antisymmetric terms with respect to a permutation of the Cartesian indices α and β .

Similar to the treatment of the spin-lattice coupling parameters [33, 34] the KKR-GF formalism allows to express the parameters $\vec{\mathcal{P}}_{ij,k}^{\alpha\beta} = (\mathcal{P}_{ij,k}^{\alpha\beta,x}, \mathcal{P}_{ij,k}^{\alpha\beta,y}, \mathcal{P}_{ij,k}^{\alpha\beta,z})$ in terms of the KKR scattering path operator matrix $\underline{\mathcal{T}}_{ij}(E)$

as follows

$$\begin{aligned} \vec{\mathcal{P}}_{ij,k}^{\alpha\beta} = & -\frac{1}{2\pi} \frac{1}{\Omega_{\text{u.c.}}} \text{Im} \text{Tr} \int dE \\ & \times \left[\langle Z^k | e \vec{r} | Z^k \rangle \underline{\mathcal{T}}_{ki} \underline{\mathcal{T}}_i^\alpha \underline{\mathcal{T}}_{ij} \underline{\mathcal{T}}_j^\beta \underline{\mathcal{T}}_{jk} \right. \\ & \left. + \langle Z^k | e \vec{r} | Z^k \rangle \underline{\mathcal{T}}_{kj} \underline{\mathcal{T}}_j^\beta \underline{\mathcal{T}}_{ji} \underline{\mathcal{T}}_i^\alpha \underline{\mathcal{T}}_{ik} \right], \end{aligned} \quad (8)$$

with $\hat{\tau}_{ij}(E)$ standing for the scattering path operator that transfers an electronic wave coming in at site j into a wave going out from site i with all possible intermediate scattering events accounted for. Using the relativistic spin-angular representation [35], the elements of the matrix $\underline{\mathcal{T}}_i^\alpha$ are given by the expression

$$T_{i,\Lambda'\Lambda}^\alpha = \int_{\Omega_q} d^3 r Z_{\Lambda'}^{i\times}(\vec{r}, E) [\beta \sigma_\alpha B_{\text{xc}}(r)] Z_\Lambda^i(\vec{r}, E), \quad (9)$$

and for the elements of the matrix $\langle Z^k | e \vec{r} | Z^k \rangle$ one has

$$\langle Z^k | e \vec{r} | Z^k \rangle_{\Lambda'\Lambda} = \int_{\Omega_q} d^3 r Z_{\Lambda'}^{k\times}(\vec{r}, E) (e \vec{r}) Z_\Lambda^k(\vec{r}, E), \quad (10)$$

where the four-component wave functions $Z_\Lambda^i(\vec{r}, E)$ stand for the regular solutions of the single-site Dirac equation with the Hamiltonian set up within the framework of relativistic spin-density functional theory [36–38] with $\Lambda = (\kappa, \mu)$, and κ and μ being the spin-orbit and magnetic quantum numbers, β is one of the standard Dirac matrices [35] and $B_{\text{xc}}(r)$ is the spin dependent part of the exchange-correlation potential. Note that the energy dependence of the scattering path operator and of the matrices $\underline{\mathcal{T}}_i^\alpha$ is omitted in Eq. (8).

By making a decomposition of the polarization parameters into symmetric $\mathcal{P}_{ij,k}^{\nu,s}$ and antisymmetric $\vec{\mathcal{P}}_{ij,k}^{\nu,a}$ parts, one gets access to the following parametrization of the electric polarization induced by a spatial spin modulation

$$\begin{aligned} \Delta P_k^\nu = & \sum_{ij} \left[\mathcal{P}_{ij,k}^{\nu,s} \{(\hat{s}_i \cdot \hat{s}_j) - \hat{s}_i^z \hat{s}_j^z\} \right. \\ & \left. + \vec{\mathcal{P}}_{ij,k}^{\nu,a} \cdot (\hat{s}_i \times \hat{s}_j) + \hat{s}_i \underline{\Pi}_{ij,k}^\nu \hat{s}_i \right]. \end{aligned} \quad (11)$$

This approach allows now a general description of the ME effect, giving in particular access to the properties of various compounds avoiding the restrictions caused by phenomenological Hamiltonians (see also discussions by Solovyev et al. [11]). This concerns, in particular, the model used to describe the ME effect depending exclusively on the leading exchange mechanism (i.e. direct exchange, superexchange, etc.), while for some materials the exchange interactions may be determined by several mechanisms competing with each other. For instance,

two competing types of Cr-Cr exchange interactions are discussed in the case of the TLA compounds $Me\text{CrO}_2$, namely, the FM superexchange and AFM direct exchange [39–41].

Furthermore, it is pointed out, that the parameters $\mathcal{P}_{ij,k}^{\nu,s}$ and $\tilde{\mathcal{P}}_{ij,k}^{\nu,a}$ are, in general, three-site parameters. They supply the information concerning the individual electric polarization of different atoms k beyond the special case of $k = i$ and $k = j$ with i and j being the site indices for the magnetic atoms with their spin moment rotated.

In the next sections we will focus on the SOC-driven polarization described by the parameters antisymmetric with respect to spin permutation, $\tilde{\mathcal{P}}_{ij,k}^{\nu,a}$. These parameters are closely connected to the DMI-like spin-lattice coupling (SLC) parameters discussed in Ref. 33 and 34, which are responsible for the forces $\mathcal{F}_k^\mu = -\sum_{\alpha,i,j} \mathcal{D}_{ij,k}^{\alpha,\mu} (\hat{e}_i \times \hat{e}_j)_\alpha$ on an atom k in the lattice, arising due to spin canting on sites i and j . These forces appear as a consequence of the electric dipole moments induced on the sites k (see Eq. (2)). Their competition with the elastic interatomic forces may lead (as discussed in Ref. 29), or may not lead to atomic displacements. In the former case, the induced local polarization is modified due to the contribution caused by the atomic displacements and can be treated as the generalized inverse-DMI mechanism. Although this impact is not taken into account in the present work, the discussed polarization mechanism is seen as a primary spin-induced polarization effect, i.e. as a counterpart of the inverse-DMI mechanism caused by atomic displacements.

III. COMPUTATIONAL DETAILS

All calculations are performed using the fully relativistic KKR Green function method [42, 43]. The exchange-correlation potential is determined within the framework of the general gradient approximation (GGA) to density functional theory (DFT), using the Perdew-Burke-Ernzerhof (PBE) parametrization [44]. A cutoff $l_{max} = 3$ was used for the angular momentum expansion of the Green function. Further details can be found for example in Refs. 34 and 45.

IV. RESULTS

Here, we present several examples for an application of our approach to deal with the ME effect for real materials. These are insulating antiferromagnets with the crystal structure having inversion symmetry. Considering the collinear magnetic state (FM or AFM) as a reference state, these materials do not exhibit any electric polarization, as it is forbidden by symmetry. However, polarization appears when the alignments of the atomic spin moments become non-collinear.

1. Cr_2O_3

As a first example, we consider the magnetoelectric properties of Cr_2O_3 , a prototypical material exhibiting the linear ME effect [12, 46–48]. Cr_2O_3 crystallizes in the corundum structure transforming according to the $R\bar{3}c$ space group [49]. Below $T_N = 310$ K it has an AFM structure with an alternating 'up-down-up-down' (' $udud$ ') alignment of the Cr spin moments parallel to the hexagonal c axis of the crystal (or alternatively, the rhomboidal $\langle 111 \rangle$ direction) [12]. Induced electric (\vec{P}) or magnetic (\vec{M}) polarization in the crystal appears as a linear response to an applied magnetic \vec{H}_{ext} or electric \vec{E}_{ext} field, respectively. The induced polarization is described by the magnetoelectric tensor $\underline{\alpha}$ defined as $\alpha_{\mu\nu}^H = (\partial P_\mu / \partial H_{\text{ext},\nu})$ in the former and $\alpha_{\mu\nu}^E = \mu_0 (\partial M_\mu / \partial E_{\text{ext},\nu})$ in the latter case, with only diagonal elements being non-zero, $\alpha_{xx} = \alpha_{yy} = \alpha_\perp$ and $\alpha_{zz} = \alpha_{||}$ (see, e.g. [14, 47, 50]). On a microscopic level, the ME tensor can be obtained on the basis of the DFT, calculating the response either to magnetic or to electric external fields, respectively.

Here we discuss the ME effect of Cr_2O_3 in terms of the parametrization scheme given in Section II. We focus on the contributions described by the parameters $\mathcal{P}_{ij,k}^{\alpha\nu,a}$, which are antisymmetric w.r.t. spin permutation. The parameters are calculated making use of Eq. (8), and then applied to the calculation of the electric polarization induced by an external magnetic field via Eq. (7). The latter step implies spin rotations for the Cr atoms on sites i by an angle Θ_i according to $(\sin(\theta_i), 0, \cos(\theta_i))$, seen as a consequence of an applied magnetic field $\vec{H}_{\text{ext}} = (H_x, 0, 0)$. The electric polarization of the unit cell is obtained as a response to such spin rotations, by summing over all induced dipole moments on 'magnetic' (Cr) as well as on 'non-magnetic' (O) atoms, according to the expression in the Eq. (7). When the magnetic field is assumed to be applied along the x direction, the non-zero contribution to the polarization stems from the parameters $\mathcal{P}_{ij,k}^{y\nu,a}$ (i.e. the component parallel to $\hat{s}_i \times \hat{s}_j$) with the index ν indicating the components of the polarization vector.

The results obtained this way are shown in Fig. 1, where the polarization components P^x, P^y and P^z for different Cr sublattices are plotted in panels (b) and (d) as a function of the tilting angle θ . Panels (a) and (c) show schematically the orientation of the polarization vectors in the unit cell. Note that we consider here as an example, two types of the AFM spin alignment in the unit cell, following the discussions in Ref. 28. Fig. 1(a),(b) represents the results for the system with the ground state spin configuration ' $udud$ ', which is invariant w.r.t. the combined \mathcal{IT} symmetry operation. One can see an identical polarization of the Cr1 and Cr3 atoms which differ from the polarization of the Cr2 and Cr4 atoms due to the opposite sign of their P^y components. However, the sum over all Cr atoms in the unit cell is

finite and negative, while the P^z component is equal to 0 for all atoms. Furthermore, the solid brown line in Fig. 1(b) represents the total polarization in the unit cell accounting for the contributions from the O atoms, indicating a strong enhancement coming from the induced O dipole moments.

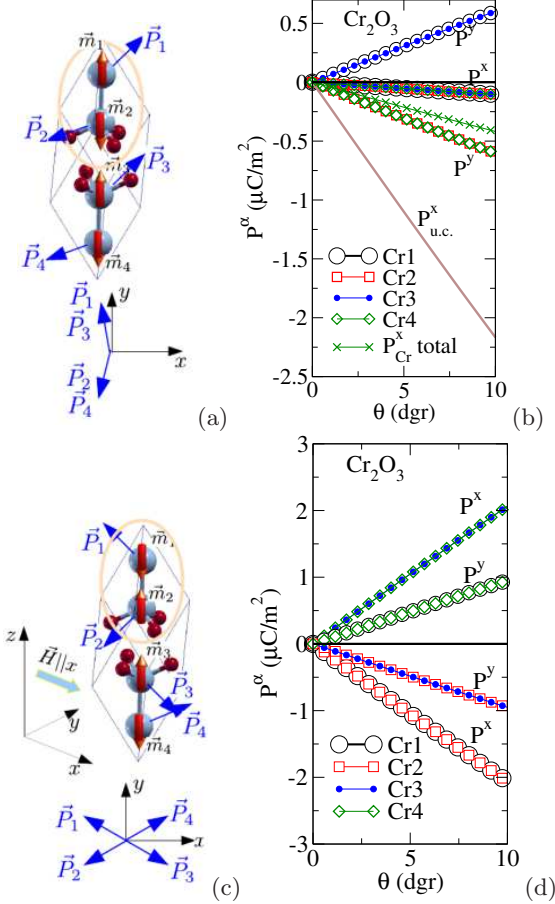


FIG. 1. Element-resolved induced electric polarization in Cr_2O_3 for the spin configurations 'udud' (upper panel) and 'duud' (lower panel) (see text). Panels (b) and (d) show the P^x and P^y components of the induced dipole moments on Cr atoms represented as a function of the tilting angle θ . Panels (a) and (c) show schematically the orientation of the polarization vectors in the unit cell (blue arrows).

The down-up-up-down ('duud') spin alignment (see Fig. 1(c),(d)) corresponds to the system invariant w.r.t. the inversion operation \mathcal{I} , for which the electric polarization should be forbidden by symmetry. This is seen in Fig. 1(c) showing that the induced Cr dipole moments are finite but cancel each other when summing over the unit cell, in line with the discussions by Solovyev [28]. This is expected from symmetry considerations, as this spin configuration ensures that the field-induced spin rotations do not break inversion symmetry in the system.

In order to demonstrate the site-resolved contributions to the unit cell electric polarization arising due to Cr spin rotations, Fig. 2 (top left) represents the dipole mo-

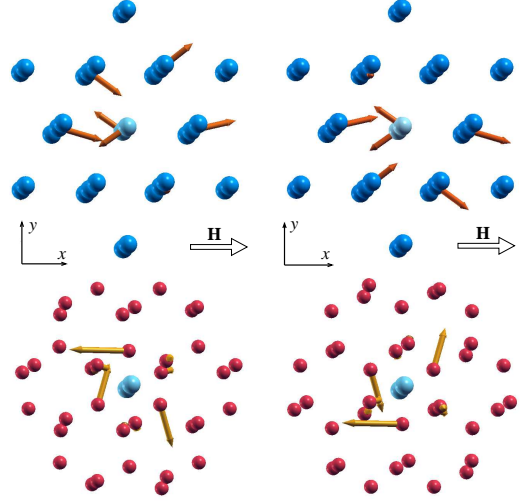


FIG. 2. Results for Cr_2O_3 with the ground-state spin configuration 'udud': arrows show the dipole moments induced on the Cr sites due to a spin rotation for the Cr1 and Cr2 atoms (top left) (i.e. the spin moments \vec{m}_1 and \vec{m}_2 shown in Fig. 1(a)) away from collinear antiferromagnetic alignment, and due to a spin rotation for the Cr3 and Cr4 atoms, i.e. \vec{m}_3 and \vec{m}_4 (see Fig. 1(a)). The arrows on the bottom left and right panels show the corresponding induced dipole moments of the O atoms.

ments for Cr_2O_3 with the ground-state spin configuration 'udud', induced on Cr sites due to spin rotations for the Cr1 and Cr2 atoms, i.e. the spin moments \vec{m}_1 and \vec{m}_2 shown in Fig. 1(a). Fig. 2 (top right) shows the Cr dipole moments due to spin rotations for the Cr3 and Cr4 atoms, i.e. \vec{m}_3 and \vec{m}_4 . Corresponding dipole moments induced on the O atoms are shown in Fig. 2 (bottom), left and right, respectively. One can see a rather strong polarization of the O atoms, which is comparable with the polarization of Cr. Furthermore, for some atoms all three components of the induced dipole moments may be non-zero. Summing up over all rotated Cr spin moments on sites i and j , one obtains the dipole moments for the Cr and O atoms corresponding to different sublattices, $\vec{P}^{Cr_i} = (P_x^{Cr_i}, P_y^{Cr_i}, 0)$ and $\vec{P}^{O_i} = (P_x^{O_i}, P_y^{O_i}, 0)$. Corresponding results for \vec{P}^{Cr_i} are plotted in Fig. 1(b) and (d) as a function of the tilting angle θ (or alternatively - as a function of strength of the magnetic field $\vec{H}_{ext}||\hat{x}$).

Coming back to the ground state 'udud' spin configuration, one can estimate the element α_{\perp} of the ME tensor. This requires to know the induced spin canting angle corresponding to an applied magnetic field, which can be estimated using the calculated exchange coupling parameters. The equilibrium condition following from the Heisenberg Hamiltonian in the presence of an external magnetic field leads to the spin tilting angle given by the expression $\theta = M H_{ext}/J_0^{ab}$, with $J_0^{ab} = \sum_j J_{0j}^{ab}$ and J_{0j}^{ab} the parameters determined by the exchange interactions between the Cr atoms which belong to the AFM-aligned Cr sublattices. The calculated exchange coupling param-

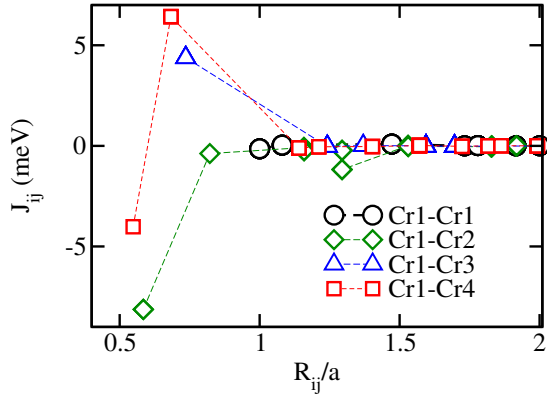


FIG. 3. The Cr-Cr exchange interactions in Cr_2O_3 as a function of the Cr-Cr distance $R_{0j}^{Cr_a-Cr_b}$.

eters between the Cr atoms corresponding to different sublattices are plotted in Fig. 3. Negative Cr1-Cr2 and Cr1-Cr4 interactions lead to the AFM ordering of the corresponding sublattices. The mean field estimate for the Néel temperature, using these exchange coupling parameters, gives the value $T_N^{MF} = 322$ K, with the parameters $J_0^{Cr1-Cr2} = J_0^{Cr1-Cr4} \approx -15$ meV, corresponding to an AFM-alignment of the Cr sublattices. With the latter quantity and the calculated Cr spin moment $M = 2.5\mu_B$, one can estimate the elements α_\perp of the ME tensor using the polarization shown in Fig. 1(b). This leads to the value $\alpha_\perp \approx -1.39$ ps/m, if the estimation is based on the total polarization per unit cell, which is in line with the experimental results as well as with other DFT-based results reported in the literature [14] (see also the references therein). Note that the estimation based on the polarization of the Cr sublattices only gives $\alpha_\perp \approx -0.28$ ps/m, which is substantially smaller and underestimates the available experimental data.

2. MnI_2

The next system we are going to consider is MnI_2 with the high-temperature phase having space group $P\bar{3}m1$ also including inversion symmetry. The Mn atomic layers create a 2D triangular lattice with AFM inter-atomic interactions. This leads to a sequence of magnetic phase transitions upon cooling, first at $T_{N1} = 3.95$ K (to the non-collinear magnetic state with a proper screw spin modulation), then at 3.8 K (T_{N2}) and 3.45 K (T_{N3}) [51]. The in-plane electric polarization of about $84 \mu\text{C}/\text{m}^2$ emerges in the proper screw magnetic ground state below T_{N3} , and is characterized by the propagation vector $\vec{q}_{m3} = (0.181, 0, 0.439)(2\pi/a)$ [27, 52].

We calculated the parameters $\mathcal{P}_{i,j,k}^{\alpha\nu,a}$ for MnI_2 , which have then been used to determine the electric polarization in the presence of proper screw spin spirals. The polarization is plotted in Fig. 4(a) and (b) as a function of the angle $\Theta = (\vec{q} \cdot \vec{R}_{01})$, where $\vec{R}_{01} = (0.866, 0.5, 0)a$

corresponds to the position of one of the nearest-neighbor Mn atoms, for two directions of the propagation vector: $\vec{q}_1 \parallel \langle 1\bar{1}0 \rangle$ (a) and $\vec{q}_2 \parallel \langle 110 \rangle$ (b) (i.e., the x and y directions, respectively, as shown in Fig. 4(c) and (d)). These directions of the MnI_2 crystal lattice are characterized by different symmetry: the $[110]$ crystallographic axis is a two-fold rotation axis while the plane including the $[1\bar{1}0]$ and the $[001]$ axes (perpendicular to the two-fold rotation axis) is a mirror plane. Due to the different symmetry properties of the two spin spirals considered, the properties of the induced electric polarization for the two cases are different.

For both propagation vectors \vec{q}_1 and \vec{q}_2 , the electric polarization is aligned along the $\langle 110 \rangle$ crystallographic direction, in line with previous results and discussions in the literature [27, 28, 52]. This is a consequence of the symmetry of the system in the presence of the spin spiral. Note once more that the KNB model fail to predict the electric polarization due to a proper screw spin spiral (see Refs. [27], [28] and [52]). As one can see in Fig. 4, the electric polarization of the Mn (blue line) and I (red line) sublattices are comparable in magnitude, but have a different q -dependence. Furthermore, the polarization of the sublattices changes sign together with the orientation of the propagation vector. One can see also the sign difference when comparing the polarization for the \vec{q}_1 and \vec{q}_2 vectors, assuming the same chirality for the spin modulation. Similar trends can also be seen for the total polarization shown in Fig. 4 by a dashed line; it has a maximum around $\Theta = 120^\circ$, corresponding to $\vec{q} = (1/3, 1/3, 0)(2\pi/a)$ in the case of $\vec{q} \parallel \langle 110 \rangle$ (\vec{q}_2 , Fig. 4 (b)), which is comparable to the experimental results. However, in the case of $\vec{q} \parallel \langle 1\bar{1}0 \rangle$ (\vec{q}_1 , Fig. 4 (a)), the absolute value of the polarization is substantially underestimated when compared to experiment [27] as well as the DFT calculations by Wu et al. [52], that can be partially attributed to their GGA+U based calculations, in contrast to the GGA approach for the exchange-correlation potential used in the present work. Furthermore, these authors demonstrated also the significance of the so called lattice contribution, which was not considered here.

In order to see more details of the symmetry properties of the polarization, Fig. 4 represents the parameters $\mathcal{P}_{0j,j}^{x\nu,a}$ (c) and $\mathcal{P}_{0j,j}^{y\nu,a}$ (d) for the first neighbor Mn shell around the Mn atom on site 0. Three pictures in each panel (c) and (d) show the components of the polarization vectors $\vec{P}_j^x = (\mathcal{P}_{0j,j}^{xx,a}, \mathcal{P}_{0j,j}^{xy,a}, \mathcal{P}_{0j,j}^{xz,a})$ and $\vec{P}_j^y = (\mathcal{P}_{0j,j}^{yx,a}, \mathcal{P}_{0j,j}^{yy,a}, \mathcal{P}_{0j,j}^{yz,a})$, respectively. They characterize the electric dipole moments of the Mn atoms appearing for each pair, Mn_0 and Mn_j , due to their spin rotations. These rotations are assumed to be the same for every pair of atoms. As one can see, the induced dipole moments are non-vanishing due to locally broken inversion symmetry. However, the polarization vectors for different pairs are connected by symmetry, depending also on the directions of the spin tilting, as is shown in figures (c) and (d). In the case of a spin modulation, e.g. cy-

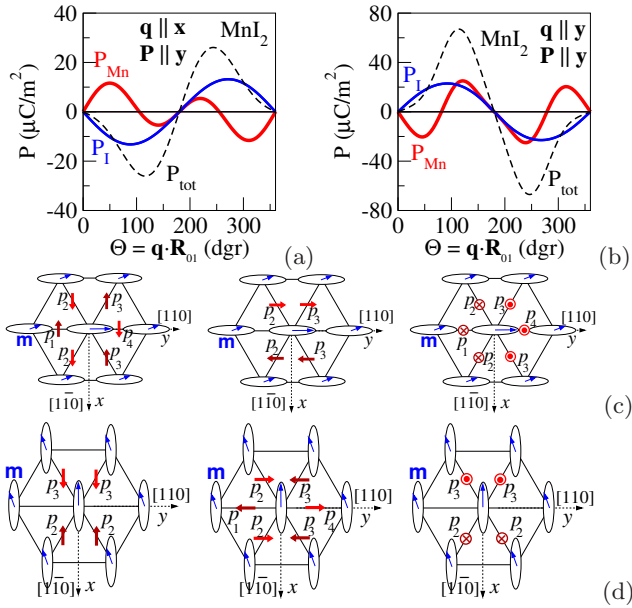


FIG. 4. Element-resolved electric polarization in MnI_2 due to proper screw magnetic structures characterized by propagation vectors $\vec{q} \parallel [110]$ (a) and $\vec{q} \parallel \langle 110 \rangle$ (b), represented as a function of the angle $\Theta = (\vec{q} \cdot \vec{R}_{01})$ where \vec{R}_{01} corresponds to the position of a nearest-neighbor Mn atom at $\vec{R}_{01} = (0.866, 0.5, 0)a$. The three plots in panels (c) and (d) represent the three components of the antisymmetric (DMI-like) electric polarization parameters $P_{ij,j}^{x\nu,a}$ (c) giving access to the electric polarization due to spin rotations within the yz plane, and the parameters $P_{ij,j}^{y\nu,a}$ (d) representing electric polarization due to spin rotations within the xz plane. The left, middle and right plots corresponding to $\nu = x, y, z$, respectively. The absolute values of the parameters in panel (c) are: (left, $\nu = x$) $|\vec{P}_2| = |\vec{P}_3| = 1.61 \mu\text{C}/\text{m}^2$, $|\vec{P}_1| = |\vec{P}_4| = 1.14 \mu\text{C}/\text{m}^2$; (middle $\nu = y$) $|\vec{P}_2| = |\vec{P}_3| = 0.38 \mu\text{C}/\text{m}^2$, $|\vec{P}_1| = |\vec{P}_4| = 0.00 \mu\text{C}/\text{m}^2$; (right $\nu = z$) $|\vec{P}_2| = |\vec{P}_3| = 0.12 \mu\text{C}/\text{m}^2$, $|\vec{P}_1| = |\vec{P}_4| = 0.33 \mu\text{C}/\text{m}^2$. The absolute values of the parameters in panel (d) are: (left, $\nu = x$) $|\vec{P}_2| = |\vec{P}_3| = 0.18 \mu\text{C}/\text{m}^2$, $|\vec{P}_1| = |\vec{P}_4| = 0.00 \mu\text{C}/\text{m}^2$; (middle $\nu = y$) $|\vec{P}_2| = |\vec{P}_3| = 1.18 \mu\text{C}/\text{m}^2$, $|\vec{P}_1| = |\vec{P}_4| = 1.99 \mu\text{C}/\text{m}^2$; (right $\nu = z$) $|\vec{P}_2| = |\vec{P}_3| = 0.27 \mu\text{C}/\text{m}^2$, $|\vec{P}_1| = |\vec{P}_4| = 0.00 \mu\text{C}/\text{m}^2$.

cloidal, or proper screw spin spirals discussed here, which are characterized by the propagation vectors \vec{q}_1 and \vec{q}_2 , some polarization contributions cancel each other. The total result depends on the type of spin spiral as well as on the direction of the \vec{q} vector. In the case of the proper screw spin modulation considered here the results shown in Fig. 4(a) and (b) demonstrate that the polarization vanishes along the directions parallel to $[001]$ and $[1\bar{1}0]$ for both propagation vectors $\vec{q}_1 \parallel [1\bar{1}0]$ (a) and $\vec{q}_2 \parallel \langle 110 \rangle$ (b). At the end, the spin spiral with \vec{q}_1 and spin rotation within the xz plane breaks the mirror symmetry w.r.t. the xz plane, leading to a finite polarization along the y (or $[110]$) axis. Similarly, the spin spiral with \vec{q}_2 and spin rotation within the zy plane breaks the 2-fold symmetry with the rotation axis parallel to the y axis, leading again

to a finite polarization along the y ($[110]$) axis.

3. MnO_2

Next, we consider shortly MnO_2 crystallized in the rutile structure with the space group $P4_2/mnm$. Previously, it was shown [28], that the total polarization of the unit cell in this material follows the symmetry constraints suggested by the KNB model. Experimentally, it was found that the system has a magnetic phase transition below $T_N \approx 92$ K to a non-collinear magnetic state with a spin spiral propagating along the tetragonal c axis [53]. For symmetry reasons [28], it does not exhibit an induced electric polarization along this axis, which is in line with the KNB model.

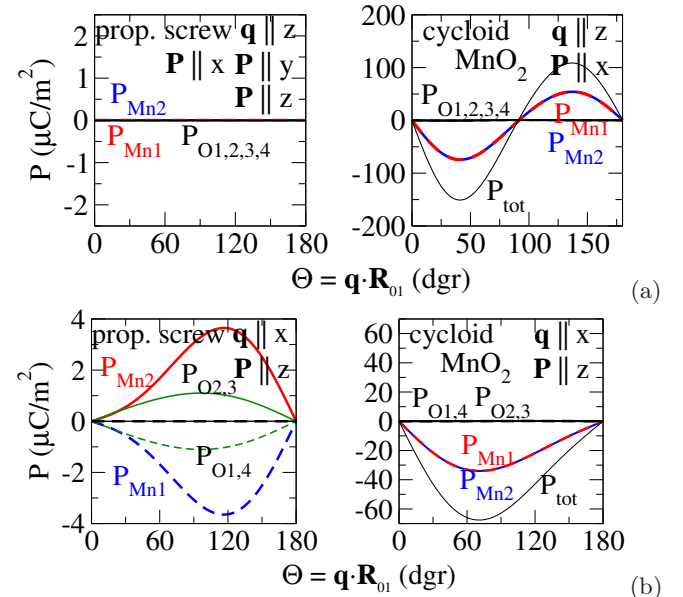


FIG. 5. The element resolved electric polarization for MnO_2 for a proper screw (left panel) and cycloidal (right panel) spin modulation with the propagation vector $\vec{q} \parallel \hat{z}$ (a) and $\vec{q} \parallel \hat{y}$ (b). In the case of a cycloidal spin modulation, the spin moments are rotated within the xz plane for $\vec{q} \parallel \hat{z}$ and within the yz plane for $\vec{q} \parallel \hat{y}$. The results are presented as a function of the angle $\Theta = \vec{q} \cdot \vec{R}_{01}$ between the nearest neighbor spin moments connected by the radius-vector \vec{R}_{01} , with the nearest neighbor atoms located at $\vec{R}_{01} = (\pm 0.5, \pm 0.5, \pm 0.327)a$.

Using the magnetic structure observed experimentally for MnO_2 , we have performed corresponding calculations of the electric polarization induced by a proper screw spin spiral propagating along the c (having four-fold rotation symmetry; $c \parallel z$ for the present settings) and y (having two-fold rotation symmetry) axes, making use of the parameters $P_{ij,j}^{\alpha\nu,a}$. The results are shown in Fig. 5(a) and (b), respectively, by the left hand panels. As one can see, no dipole moment is induced due to the spin spiral with $\vec{q} \parallel \hat{z}$, while in the case of a propagation vector along the two-fold axis, $\vec{q} \parallel \hat{y}$, the dipole moments are induced

along the z axis, having opposite sign for the Mn1 and Mn2 atoms. The same trend is obtained also for the O atoms. Two of them, O1 and O4, have the same dipole moment, and for the two others, O2 and O3, the dipole moment is opposite to the first two. As a result, summation over all contributions leads to zero polarization due to a canceling of all contributions in the unit cell. On the other hand, the results are different in the case of a cycloidal spin modulation having the same propagation direction as for the proper screw spin spirals, i.e. along the z and y axes. In the first case the spin moments are rotated within the xz plane and in the second case within the yz plane. The results are shown in Fig. 5(a) and (b), respectively, on the right hand panels. In both cases the polarization of the O sublattices is almost vanishing, while the polarization is finite and identical for both Mn sublattices, leading to a finite total polarization. This is oriented along the directions perpendicular to the propagation vectors, i.e. $\vec{P} \parallel \hat{x}$ for $\vec{q} \parallel \hat{z}$ (a) and $\vec{P} \parallel \hat{z}$ for $\vec{q} \parallel \hat{y}$. This finding, again, is in line with the prediction of the KNB model.

4. $CuCrO_2$ and $AgCrO_2$

As another example for TLA materials we are going to discuss the compounds $CuCrO_2$ and $AgCrO_2$ seen as representatives of the $MeFeO_2$ and $MeCrO_2$ oxides. For these materials a first-principles treatment of a spin-induced electric polarization (i.e. beyond the phenomenological model consideration) may be challenging because of the competition of two mechanisms of nearest-neighbor exchange interactions, i.e. the FM superexchange and AFM direct exchange. One can expect a corresponding competition also for the magnetoelectric polarization. At room temperature these materials crystallize in the delafossite crystal structure having $R\bar{3}m$ space group symmetry. Their magnetic properties are essentially determined by frustrated antiferromagnetic exchange interactions [17, 54]. However, we do not discuss here the mag-

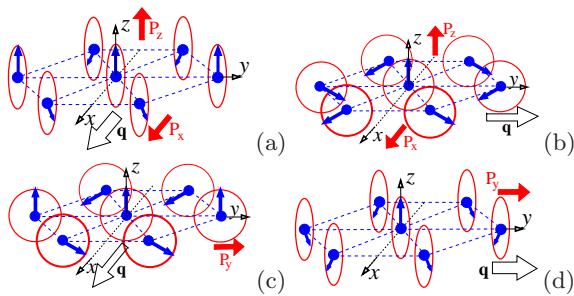


FIG. 6. Spin modulation in a 2D triangular lattice: cycloidal with $\vec{q} \parallel \hat{x} \parallel [1\bar{1}0]$ (a) and with $\vec{q} \parallel \hat{y} \parallel [110]$ (b); and a proper screw spiral with $\vec{q} \parallel \hat{x} \parallel [1\bar{1}0]$ (c) and with $\vec{q} \parallel \hat{y} \parallel [110]$ (d). The red arrows show the possible orientations of the electric polarization corresponding to the spin configuration on each panel (a), (b), (c) or (d).

netic ordering in these materials, but only stress that the non-collinear AFM structure at low temperature is accompanied by an emerging electric polarization, similar to the TLA MnI_2 compound.

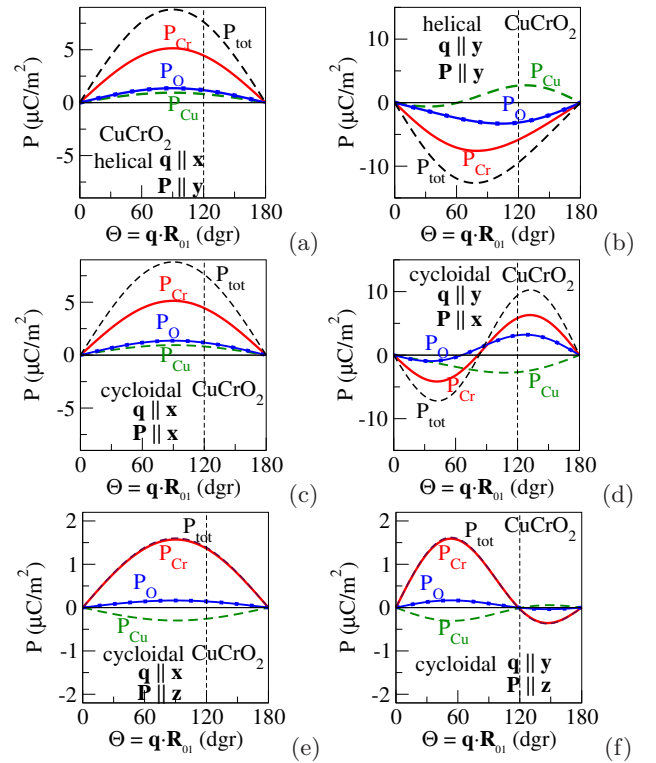


FIG. 7. The $\vec{P}_{ijk}^{\nu,a}$ -related electric polarization for the $CuCrO_2$ compound: on Cu sites (green), Cr sites (red) and O sites (blue). Panels (a) and (b) show the polarization induced by a proper screw spin modulation characterized by the wave vector $\vec{q} \parallel \hat{x} \parallel [1\bar{1}0]$ and $\vec{q} \parallel \hat{y} \parallel [110]$, respectively. In both cases a polarization emerges along the y direction. Panels (c) and (e) show the x and z components of the polarization induced by a cycloidal spin modulation characterized by the wave vector $\vec{q} \parallel \hat{x}$. Panels (d) and (f) show the x and z polarization components for a cycloidal spin modulation with $\vec{q} \parallel \hat{y}$, respectively. The results are presented as a function of the angle $\Theta = \vec{q} \cdot \vec{R}_{01}$ (similar to Fig. 4).

Previous neutron diffraction studies on $CuCrO_2$ propose an out-of-plane 120° chiral spin structure below $T_N \sim 24$ K, as the ground state, with a propagation vector $\vec{q} = (1/3, 1/3, 0)(2\pi/a)$ [55] and incommensurate $\vec{q} = (0.329, 329, 0)(2\pi/a)$ (either a helicoidal or cycloidal) [56], while an incommensurate proper-screw magnetic structure was suggested in Ref. 57. The observed spontaneous electric polarization appearing below T_N can be attributed to the non-collinear magnetic structure indicating the coupling between the ferroelectricity and spiral magnetic order [25, 57-60]. Note, however, that magnetic fields above 5.3 T, applied along the Cr (xy) plane, can induce a transition to a cycloidal spin structure [61]. Therefore, we calculated the electric polarization induced in $CuCrO_2$ both by the proper-screw as well as by cy-

cloidal spin spirals with the propagation vectors along the $\langle 110 \rangle$ and $\langle \bar{1}\bar{1}0 \rangle$ directions. The results for CuCrO_2 are shown in Fig. 7 as a function of the angle Θ (see the definition given above). In the case of a proper-screw spin spiral, the non-zero polarization occurs in contrast to the prediction by the phenomenological KNB model [21] for the propagation vector $\vec{q} \parallel [110]$, while it is orthogonal to \vec{q} , i.e. $\vec{P} \parallel [110]$ for $\vec{q} \parallel [\bar{1}\bar{1}0]$, similar to the results obtained for MnI_2 . The same trend can also be seen in Fig. 9 for AgCrO_2 . The vertical dashed line correspond to $\Theta = 120^\circ$, i.e. the angle between the nearest neighbor Cr atoms, observed experimentally. For this angle the total electric polarization per unit cell for CuCrO_2 and AgCrO_2 are close to each other. The black dashed curves in Figs. 7 and 9 give the polarization in the unit cell being a sum over all contributions of the polarization of Cu, Cr and O sublattices. As one can see, the polarization of the Cr sublattice is dominating in CuCrO_2 , while it is comparable with the polarization of the Ag sublattice in AgCrO_2 . Moreover, in the case of $\vec{q} \parallel [110]$, the polarization of the O sublattice vanishes in AgCrO_2 , in contrast to CuCrO_2 .

In all cases, the electric polarization vanishes at $\Theta = 180^\circ$, when the magnetic moments are getting collinear, changing sign due to a change of the spin spiral chirality. Occasionally, the sign change can also be seen for other angles $\Theta < 180^\circ$. In terms of the real-space three-site parameters, these sign changes can be seen as a result of a competition of the contributions to the polarization caused by spin rotations of all surrounding atoms. Interestingly, this leads to the polarization along the z direction almost vanishing at $\Theta = 120^\circ$ in the case of a cycloidal spin modulation with the propagation vector $\vec{q} \parallel [110]$. For more details we plot in Fig. 8(b) the contribution to the Cr dipole moment (central atom 0) induced along the z direction due to a rotation of the nearest neighbor Cr magnetic moments corresponding to a cycloidal spin modulation shown in Fig. 6(b). One can

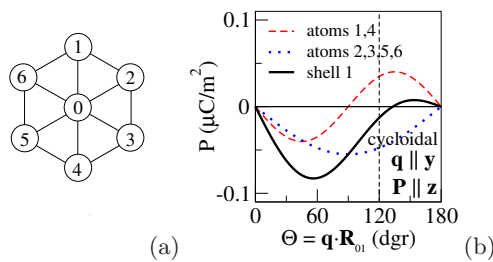


FIG. 8. (a) Cr atom (site 0) in CuCrO_2 surrounded by the nearest neighbor atoms (atoms 1–6) within the Cr layer; (b) Dipole moment on the central Cr atom with its spin moment along the z axis (perpendicular to the plane) induced by spin rotations on the atoms 1–6 (black solid line) in the case of a cycloidal spin modulation with $\vec{q} \parallel \hat{y} \parallel [110]$ shown in Fig. 6(b), seen as a contribution to the Cr dipole moment shown in Fig. 7(f). The red dashed line represents the contribution due to a rotation of atoms 1 and 4, while the dashed blue line shows the contribution due to atoms 2, 3, 5 and 6.

clearly see a significant cancellation of the dipole moment at $\Theta = 120^\circ$. When more neighbors are taken into account, one obtains the results shown in Fig. 7(f). A very similar behavior of the electric polarization is observed also for AgCrO_2 (see Fig. 9).

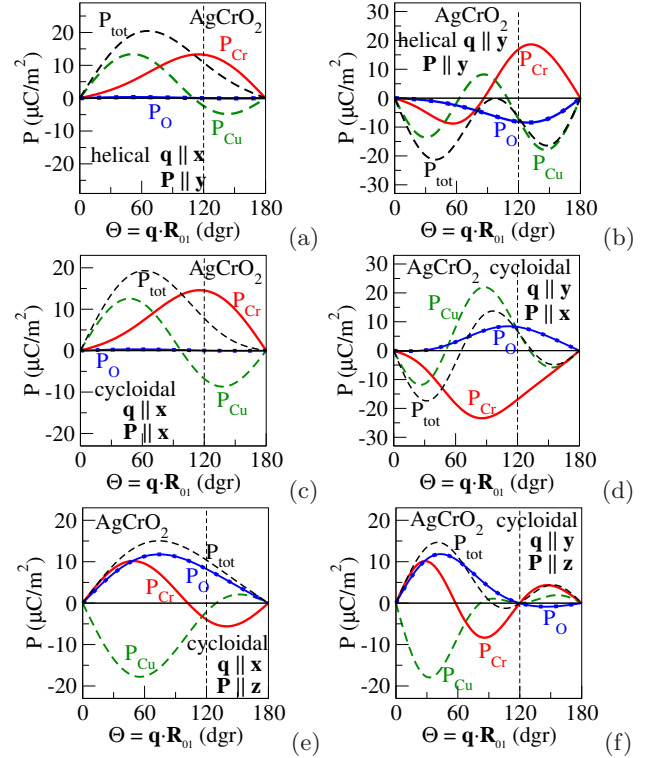


FIG. 9. The $\vec{P}_{ij,k}^{\nu,a}$ -originated electric polarization for the AgCrO_2 compound: on Ag sites (green), Cr sites (red) and O sites (blue). Panels (a) and (b) show the polarization induced by a proper screw spin modulation characterized by wave vector $\vec{q} \parallel \hat{y} \parallel [1\bar{1}0]$ and $\vec{q} \parallel \hat{y} \parallel [110]$, respectively. In both cases polarization emerges along y direction. Panels (c) and (e) show the x and z components of the polarization induced by cycloidal spin modulation characterized by wave vector $\vec{q} \parallel \hat{x}$. Panels (d) and (f) show the x and z polarization components for cycloidal spin modulation with $\vec{q} \parallel \hat{y}$, respectively. The results are presented as a function of the angle $\Theta = \vec{q} \cdot \vec{R}_{01}$ (similar to Fig. 4).

V. SUMMARY

In summary, we present in this work an approach to describe the ME effect in insulating antiferromagnets on a first-principles level. This approach may be seen as a generalization of the spin-current KNB model, giving a more complete description of the induced electric polarization in real materials. In particular, this approach leads to finite values for the electric polarization in the presence of proper screw spin spirals. This means that it accounts at least for two possible mechanisms contributing to the ME effect in TLA materials, i.e. the generalized

inverse-DMI in addition to the so-called $s-d$ hybridization mechanism suggested in the literature. Furthermore, the proposed approach gives access to the analysis of the element resolved electric polarization described by three-site parameters. It allows a further extension accounting for the on-site contribution to the polarization via the parameters seen as counterparts of the MCA-like spin-

lattice coupling parameters introduced previously [34].

VI. ACKNOWLEDGEMENTS

J.M. was supported by the project Quantum materials for applications in sustainable technologies (QM4ST), funded as project No. CZ.02.01.01/00/22_008/0004572 by P JAK, call Excellent Research.

[1] G. A. Smolenskii and I. E. Chupis, *Phys. Usp.* **25**, 475 (1982).

[2] D. Khomskii, *Physics Online J.* **2**, 20 (2009).

[3] A. P. Pyatakov and A. K. Zvezdin, *Physics-Uspekhi* **55**, 557 (2012).

[4] N. Ortega, A. Kumar, J. F. Scott, and R. S. Katiyar, *Journal of Physics: Condensed Matter* **27**, 504002 (2015).

[5] X. Liang, H. Chen, and N. X. Sun, *APL Materials* **9**, 041114 (2021).

[6] S.-W. Cheong and M. Mostovoy, *Nature materials* **6**, 13 (2007).

[7] Y. Tokura, S. Seki, and N. Nagaosa, *Reports on Progress in Physics* **77**, 076501 (2014).

[8] E. Bousquet and A. Cano, *Physical Sciences Reviews* **8**, 479 (2023).

[9] M. Mostovoy, *Phys. Rev. Lett.* **96**, 067601 (2006).

[10] M. Mostovoy, K. Nomura, and N. Nagaosa, *Phys. Rev. Lett.* **106**, 047204 (2011).

[11] I. V. Solovyev, *Condens. Matter* **10** (2025), 10.3390/condmat10020021.

[12] D. Astrov, *Sov. Phys.-JETP* **13**, 729 (1961).

[13] A. Malashevich, S. Coh, I. Souza, and D. Vanderbilt, *Phys. Rev. B* **86**, 094430 (2012).

[14] E. Bousquet, E. Lelievre-Berna, N. Qureshi, J.-R. Soh, N. A. Spaldin, A. Ururu, X. H. Verbeek, and S. F. Weber, *Journal of Physics: Condensed Matter* **36**, 155701 (2024).

[15] H. Yamaguchi, S. Ohtomo, S. Kimura, M. Hagiwara, K. Kimura, T. Kimura, T. Okuda, and K. Kindo, *Phys. Rev. B* **81**, 033104 (2010).

[16] M. Frontzek, G. Ehlers, A. Podlesnyak, H. Cao, M. Matsuda, O. Zaharko, N. Aliouane, S. Barilo, and S. V. Shiryaev, *Journal of Physics: Condensed Matter* **24**, 016004 (2011).

[17] K. Park, J. Oh, J. C. Leiner, J. Jeong, K. C. Rule, M. D. Le, and J.-G. Park, *Phys. Rev. B* **94**, 104421 (2016).

[18] Y. Oohara, S. Mitsuda, H. Yoshizawa, N. Yaguchi, H. Kuriyama, T. Asano, and M. Mekata, *Journal of the Physical Society of Japan* **63**, 847 (1994), <https://doi.org/10.1143/JPSJ.63.847>.

[19] A. M. L. Lopes, G. N. P. Oliveira, T. M. Mendonça, J. A. Moreira, A. Almeida, J. P. Araújo, V. S. Amaral, and J. G. Correia, *Phys. Rev. B* **84**, 014434 (2011).

[20] T. Kurumaji, *Physical Sciences Reviews* **5**, 20190016 (2020).

[21] H. Katsura, N. Nagaosa, and A. V. Balatsky, *Phys. Rev. Lett.* **95**, 057205 (2005).

[22] T. Kimura, T. Goto, H. Shintani, K. Ishizaka, T. Arima, and Y. Tokura, *Nature* **426**, 55 (2003).

[23] H. J. Xiang, S.-H. Wei, M.-H. Whangbo, and J. L. F. Da Silva, *Phys. Rev. Lett.* **101**, 037209 (2008).

[24] K. Taniguchi, N. Abe, T. Takenobu, Y. Iwasa, and T. Arima, *Phys. Rev. Lett.* **97**, 097203 (2006).

[25] S. Seki, Y. Onose, and Y. Tokura, *Phys. Rev. Lett.* **101**, 067204 (2008).

[26] T.-h. Arima, *Journal of the Physical Society of Japan* **76**, 073702 (2007), <https://doi.org/10.1143/JPSJ.76.073702>.

[27] T. Kurumaji, S. Seki, S. Ishiwata, H. Murakawa, Y. Tokunaga, Y. Kaneko, and Y. Tokura, *Phys. Rev. Lett.* **106**, 167206 (2011).

[28] I. V. Solovyev, *Phys. Rev. B* **95**, 214406 (2017).

[29] I. A. Sergienko and E. Dagotto, *Phys. Rev. B* **73**, 094434 (2006).

[30] H. J. Xiang, E. J. Kan, Y. Zhang, M.-H. Whangbo, and X. G. Gong, *Phys. Rev. Lett.* **107**, 157202 (2011).

[31] S. A. Nikolaev and I. V. Solovyev, *Phys. Rev. B* **99**, 100401 (2019).

[32] I. Solovyev, R. Ono, and S. Nikolaev, *Phys. Rev. Lett.* **127**, 187601 (2021).

[33] S. Mankovsky, S. Polesya, H. Lange, M. Weißenhofer, U. Nowak, and H. Ebert, *Phys. Rev. Lett.* **129**, 067202 (2022).

[34] S. Mankovsky, H. Lange, S. Polesya, and H. Ebert, *Phys. Rev. B* **107**, 144428 (2023).

[35] M. E. Rose, *Relativistic Electron Theory* (Wiley, New York, 1961).

[36] A. H. MacDonald and S. H. Vosko, *J. Phys. C: Solid State Phys.* **12**, 2977 (1979).

[37] E. Engel and R. M. Dreizler, *Density Functional Theory – An advanced course* (Springer, Berlin, 2011).

[38] H. Ebert, J. Braun, D. Ködderitzsch, and S. Mankovsky, *Phys. Rev. B* **93**, 075145 (2016).

[39] S. Angelov and J. Doumerc, *Solid State Communications* **77**, 213 (1991).

[40] I. I. Mazin, *Phys. Rev. B* **75**, 094407 (2007).

[41] A. V. Ushakov, D. A. Kukusta, A. N. Yaresko, and D. I. Khomskii, *Phys. Rev. B* **87**, 014418 (2013).

[42] H. Ebert et al., *The Munich SPR-KKR package*, version 8.5, <https://www.ebert.cup.uni-muenchen.de/en/software-en/13-sprkkr> (2020).

[43] H. Ebert, D. Ködderitzsch, and J. Minár, *Rep. Prog. Phys.* **74**, 096501 (2011).

[44] J. P. Perdew, K. Burke, and M. Ernzerhof, *Phys. Rev. Lett.* **77**, 3865 (1996).

[45] S. Mankovsky, S. Polesya, and H. Ebert, *Phys. Rev. B* **101**, 174401 (2020).

[46] I. Dzyaloshinskii, *Sov. Phys.-JETP* **10**, 628 (1960).

[47] E. Kita, K. Siratori, and A. Tasaki, *Journal of Applied Physics* **50**, 7748 (1979).

[48] E. Bousquet, N. A. Spaldin, and K. T. Delaney, *Phys. Rev. Lett.* **106**, 107202 (2011).

- [49] P. J. Brown, J. B. Forsyth, E. Lelièvre-Berna, and F. Tasset, *Journal of Physics: Condensed Matter* **14**, 1957 (2002).
- [50] A. Scaramucci, E. Bousquet, M. Fechner, M. Mostovoy, and N. A. Spaldin, *Phys. Rev. Lett.* **109**, 197203 (2012).
- [51] T. Sato, H. Kadowaki, and K. Iio, *Physica B* **213-214**, 224 (1995).
- [52] X. Wu, Y. Cai, Q. Xie, H. Weng, H. Fan, and J. Hu, *Phys. Rev. B* **86**, 134413 (2012).
- [53] A. Yoshimori, *Journal of the Physical Society of Japan* **14**, 807 (1959), <https://doi.org/10.1143/JPSJ.14.807>.
- [54] F. Ye, Y. Ren, Q. Huang, J. A. Fernandez-Baca, P. Dai, J. W. Lynn, and T. Kimura, *Phys. Rev. B* **73**, 220404 (2006).
- [55] H. Kadowaki, H. Kikuchi, and Y. Ajiro, *Journal of Physics: Condensed Matter* **2**, 4485 (1990).
- [56] M. Poienar, F. m. c. Damay, C. Martin, V. Hardy, A. Maignan, and G. André, *Phys. Rev. B* **79**, 014412 (2009).
- [57] M. Soda, K. Kimura, T. Kimura, M. Matsuura, and K. Hirota, *Journal of the Physical Society of Japan* **78**, 124703 (2009), <https://doi.org/10.1143/JPSJ.78.124703>.
- [58] K. Kimura, T. Otani, H. Nakamura, Y. Wakabayashi, and T. Kimura, *Journal of the Physical Society of Japan* **78**, 113710 (2009), <https://doi.org/10.1143/JPSJ.78.113710>.
- [59] K. Kimura, H. Nakamura, K. Ohgushi, and T. Kimura, *Phys. Rev. B* **78**, 140401 (2008).
- [60] K. Kimura, H. Nakamura, S. Kimura, M. Hagiwara, and T. Kimura, *Phys. Rev. Lett.* **103**, 107201 (2009).
- [61] E. Mun, M. Frontzek, A. Podlesnyak, G. Ehlers, S. Barilo, S. V. Shiryaev, and V. S. Zapf, *Phys. Rev. B* **89**, 054411 (2014).